arXiv:1408.3022v1 [physics.space-ph] 12 Aug 2014

First- and Second-order Fermi Acceleration at Parallel Shocks

Sandroos, A.[1]
Finnish Meteorological Institute, PO Box 503, FI-00101, Helsinki, Finland.
arto.sandroos@fmi.fi

Li, G.
Department of Physics, University of Alabama in Huntsville, Huntsville, AL 35805, USA.
and

Zhao, L.
Department of Physics, University of Alabama in Huntsville, Huntsville, AL 35805, USA.

Abstract

We report on a new Monte Carlo method for simulating diffusive shock acceleration (DSA) of solar energetic particles at upstream and downstream regions of quasi-parallel collisionless shock waves under the influence of self-generated turbulence. By way of example, we apply the model to a fast 1500 km s^{-1} coronal mass ejection at ten solar radii. Results indicate that the maximum energies at outer corona are likely to be limited to few MeV, due to lack of suprathermal protons for appreciable wave growth, and insufficient time required acceleration. We find that the second-order Fermi acceleration, although being a too slow process to have a notable effect at the highest energies, significantly flattens energy spectra at low energy end. Simulations indicate that protons continue to damp waves efficiently several solar radii from the shock in the downstream region, which may be an important mechanism for heating suprathermals. Our simulations also suggest that models assuming a simple isotropic scattering are likely to predict too efficient acceleration.

Subject headings: acceleration of particles, methods: numerical, shock waves, Sun: corona, Sun: coronal mass ejections (CMEs), Sun: particle emission

1. Introduction

Acceleration of ions by collisionless shocks driven by coronal mass ejections (CMEs) is the best developed theory for the genesis of gradual solar energetic particle (SEP) events. The underlying mechanism is the diffusive shock acceleration (DSA), in which ions scatter off waves present in the upstream and downstream regions of the shock, cross the shock multiple times, diffuse in momentum(Axford et al. 1977; Krymskii 1977; Bell 1978; Blandford and Ostriker 1978).

Effective DSA requires that the near upstream region is highly turbulent to provide enough scattering to keep ions close to the shock, otherwise ions can easily escape the acceleration region to interplanetary space without gaining much energy. In some SEP events there are enough particles to amplify the waves near the shock, sometimes even by several orders of magnitude (Ng et al. 2003; Vainio and Laitinen 2007), in which case the SEP intensities end up being streaming limited (Reames and Ng 1998). Shock drift acceleration (SDA) at oblique shocks can further speed up the acceleration (Webb et al. 1983; Jokipii 1987).

Over the years, many quantitative models have attempted to couple wave generation with DSA

[1]Space Sciences Laboratory, University of California, Berkeley, CA 94720, USA.

by employing various simplifying assumptions. Monte-Carlo models typically consider ion acceleration in a predescribed turbulence (Decker 1988; Ellison et al. 1990; Vainio et al. 2000; Giacalone 2005; Sandroos and Vainio 2006). Quasi-stationary models assume that the ions and wave spectra near the shock will quickly reach steady-state conditions (Zank et al. 2000; Li et al. 2003, 2005). Self-consistent models exist (Ng et al. 1999, 2003; Vainio and Laitinen 2007; Battarbee et al. 2011), but they are limited to one spatial dimension which limits their applicability for the solar corona, where the shock and magnetic geometry are very complex and vary with time. Very few models include the downstream region self-consistently (Ng and Reames 2008). Instead, an analytic model is typically used, e.g., probability of return method by Bell (1978), to return a fraction of transmitted particles back to the upstream region. However, detailed modeling of the wave and particle intensities both upstream and downstream of shocks is very important for the Solar Probe Plus mission, which will hopefully provide in-situ observations of SEPs while they are still being accelerated near coronal shock waves.

Corsair/SEP is a project aiming to develop a self-consistent model, in the sense of conserving the total energy of ions and waves during scattering, for DSA of SEPs at coronal shocks in multiple spatial dimensions. This allows us to take into account effects due to variations in local shock obliquity angle arising from, e.g., inhomogeneous coronal magnetic field and/or curved shock surface (Tylka and Lee 2006; Sandroos and Vainio 2006, 2007), to model longitudinal distribution of SEP intensities, and study how they change over time.

The purpose of this manuscript is to introduce and validate the numerical DSA model implemented in Corsair/SEP code. We apply it to DSA at parallel shocks using parameters that are suitable for solar corona near ten solar radii, and discuss the self-generated wave spectra in detail.

The manuscript is organized as follows: Section 2 presents the numerical model in detail, divided into subsections giving an overview of the simulation (Sections 2.1-2.2), model for ambient plasma and suprathermals (Section 2.3), Alfvén waves (Section 2.4) and their growth (Section 2.6), and ion propagation and pitch-angle scattering (Section 2.5). In Section 3 we compare the code against a few test cases. Results for DSA at parallel shocks are presented and discussed in Section 4. Section 5 ends the manuscripts with a summary.

2. Numerical Model

2.1. Overview Of Simulation

A summary of simulation propagation loop in pseudocode is given below for reference. The individual steps and underlying physics are documented in Sections 2.2-2.7.

```
for each timestep
1. Re-evaluate global time step
2. Scattering
  2.1. accumulate wave packet energies
  2.2. convert wave energy
       density to intensity
  2.3. scatter particles and
       accumulate growth factors
  2.4. apply wave growth
3. Propagation
  3.1. propagate particles
  3.2. propagate wave packets
  3.2. apply boundary conditions
4. inject new particles
   and wave packets
5. Particle Splitting
```

2.2. Simulation Mesh

In Corsair/SEP waves and protons are modeled using macroparticles. A two-dimensional (x, λ) phase-space mesh is used to mediate wave-particle interactions. The phase-space mesh is further split into a one-dimensional mesh in configuration space (x coordinate, i index) with uniform cell size Δx and volume Δx^3. Each spatial cell contains a wavelength mesh (λ coordinate, l index) with uniform cell size in logarithmic units, $\ln \Delta\lambda = \ln(\lambda_{l+1} - \lambda_l)$, where λ_l are the node coordinates. A cell having indices (i, l) covers the phase-space $[x_i, x_{i+1}) \times [\lambda_l, \lambda_{l+1})$ in physical coordinates, $[i, i+1) \times [l, l+1)$ in logical coordinates.

We use λ instead of the wave number $k = 2\pi/\lambda$ to simplify scattering across pitch (pitch angle cosine) $\mu = 0^{\pm}$ – ions cross $\lambda = 0$ point instead of $k = \pm\infty$. A convention that positive (negative) λ correspond to left-handed L (right-handed R) wave helicities is used.

Simulation uses logical coordinates instead of physical ones. For an ion in position x, the corre-

sponding logical coordinate is $x_{\rm L} = (x - x_0)/\Delta x$, i.e., the i-index of the spatial cell in which the particle currently resides is given by the integer part of $x_{\rm L}$. Logical wavelength coordinate is

$$\lambda_{\rm L} = \begin{cases} N_\lambda/2 - \max\left(0, \ln|\lambda/\lambda_0|\right), & \lambda < 0, \\ N_\lambda/2 + \max\left(0, \ln\lambda/\lambda_0\right), & \lambda \geqslant 0, \end{cases} \quad (1)$$

where N_λ is the (even) number of cells in wavelength mesh. Linear units are used for the two cells neighboring $\lambda = 0$ point, $|\lambda| \leqslant \lambda_0$, to improve mesh resolution at longer wavelengths.

Interpolations and accumulations between particle positions and the phase-space mesh are carried out in logical coordinates, using particle shape factors commonly used in particle-in-cell methods (e.g., Birdsall and Langdon 1985; Hockney and Eastwood 1989). For example, in one dimension, triangular-shaped clouds (TSC) interpolate a scalar quantity ϕ from mesh to position $x_{\rm L}$ using the values $\phi_{\rm i-1}$, $\phi_{\rm i}$, $\phi_{\rm i+1}$ from nearest cells as $\phi(x_{\rm L}) = \sum S_{\rm n}\phi_{\rm n}$, where

$$S_{\rm n} = \begin{cases} ({\rm i} + 1 - x_{\rm L})^2/2 & \text{for n =i} - 1, \\ (x_{\rm L} - {\rm i})^2/2 & \text{for n =i} + 1, \\ 1 - S_{\rm i-1} - S_{\rm i+1} & \text{for n =i}, \\ 0 & \text{otherwise.} \end{cases}$$

In two dimensions the interpolated value is simply the product of one-dimensional shape factors, $\phi(x_{\rm L}, \lambda_{\rm L}) = \sum S_n S_m \phi_{nm}$. Henceforth we will drop the summation symbols and use a short-hand notation $S_{\rm i} S_{\rm l} \phi_{\rm il} = S_{\rm il}\phi_{\rm il}$.

2.3. Ambient Plasma Model

Simulations are carried out in the shock normal incidence frame. In the upstream region (subscript 1) plasma has a constant mass density $\rho_{\rm m1}$, speed $V_{\rm n1}$, and magnetic field $B_{\rm n1}$. Plasma parameters in the downstream region (subscript 2) are solved using ideal MHD Rankine-Hugoniot equations,

$$\begin{aligned} \frac{\rho_{\rm m2}}{\rho_{m1}} &= r, \\ \frac{V_{\rm n2}}{V_{\rm n1}} &= r^{-1}, \\ \frac{B_{\rm n2}}{B_{\rm n1}} &= 1, \\ \frac{p_2}{p_1} &= \frac{(\gamma+1)\,r - (\gamma-1)}{(\gamma+1) - (\gamma-1)\,r}, \end{aligned}$$

where $\gamma = 5/3$ is the polytropic index, r is the gas compression ratio, p is the pressure, and subscript n refers to normal component with respect to shock normal.

Suprathermal ions are assumed to have a Kappa distribution in energy U,

$$f_\kappa(U) = \frac{C_\Gamma}{\kappa U_\kappa}\sqrt{\frac{U}{\kappa U_\kappa}}\left(1 + \frac{U}{\kappa U_\kappa}\right)^{-(\kappa+1)}, \quad (2)$$

where

$$C_\Gamma = \frac{\Gamma(\kappa+1)}{\Gamma(\kappa - \frac{1}{2})\Gamma(\frac{3}{2})}, \quad (3)$$

$$U_\kappa = \left(\frac{2\kappa - 3}{2\kappa}\right) k_{\rm B} T. \quad (4)$$

Here T is plasma Maxwell-Boltzmann temperature, and κU_κ is thermal energy in kappa distribution. We assume ion distributions to be isotropic in momentum space.

2.4. Alfvén waves

We model Alfvén waves propagating parallel (superscript +) and antiparallel (superscript −) to ambient magnetic field as monochromatic wave packets, each carrying the total (electric + magnetic) energy in waves over a wavelength range,

$$U_{\rm packet} = \frac{1}{\mu_0}\int d^3\mathbf{r} \int_{\lambda_{\rm min}}^{\lambda_{\rm max}} \delta B^2(\mathbf{r}, \lambda) d\lambda, \quad (5)$$

where $\delta\mathbf{B}$ is the perturbed magnetic field.

Wave packets are propagated using WKB raytracing equations (e.g., Whitham 1965),

$$\frac{d\mathbf{R}^{\pm}_{\mathrm{L,R}}}{dt} = \mathbf{V}_{\mathrm{w}} = \mathbf{V}_{\mathrm{p}} \pm \mathbf{V}_{\mathrm{A}}, \quad (6)$$

$$\frac{d\log(\lambda^{\pm}_{\mathrm{L,R}})}{dt} = \frac{d}{dr}\left(\mathbf{V}_{\mathrm{p}} \pm \mathbf{V}_{\mathrm{A}}\right), \quad (7)$$

$$\mathbf{V}_{\mathrm{A}} = \mathbf{B}_0/\sqrt{\mu_0 \rho_m}, \quad (8)$$

where $\mathbf{V}_{\mathrm{p}}$ and $\mathbf{V}_A$ are the plasma and Alfvén velocities at position $\mathbf{R}$, and $\mathbf{B}_{\mathrm{o}}$ is the ambient magnetic field. Henceforth the subscripts L and R, and superscripts $\pm$, are dropped whenever the intention is clear.

Alfvén waves are assumed to have a power-law spectral intensity $I(k) = I_0(k/k_0)^{\sigma}$ in the ambient coronal plasma. The corresponding wavelength spectrum can be calculated using the relation

$$I(\lambda)d\lambda = I(k)dk = \frac{k^2}{2\pi} I(k)d\lambda. \quad (9)$$

Thus, if the k-spectrum has a spectral index σ, the spectral index of λ-spectrum is $s = \sigma + 2$. Intensity is related to total wave energy density as

$$U_{\mathrm{w,tot}} = \frac{\delta B^2}{\mu_0} = \frac{1}{\mu_0}\int I(\lambda)d\lambda. \quad (10)$$

Finally, we normalize wave energy densities to energy density of ambient magnetic field,

$$\frac{1}{\mu_0}\int I^{\pm}_{\mathrm{L,R}}(\lambda)d\lambda = C^{\pm}_{\mathrm{L,R}} \cdot \frac{B_0^2}{2\mu_0}, \quad (11)$$

where $C^{\pm}_{\mathrm{L,R}} < 1$ is a constant.

Each time step, wave packet energies are accumulated to the phase-space mesh to form wave spectral energy $U_{\mathrm{w}}(\mathbf{r}, \lambda)$. Each phase-space cell neighboring a wave packet's position receives a value $U_{\mathrm{w},il} = S_{il} U_{\mathrm{packet}}$. The obtained $U_{\mathrm{w}}(\mathbf{r}, \lambda)$ is then converted into intensity in preparation for the scattering step,

$$I_{\mathrm{il}} = \mu_0 U_{\mathrm{w,il}} / \left(\Delta x^3 \Delta\lambda_{\mathrm{l}}\right). \quad (12)$$

2.4.1. Injection

New wave packets are injected to the spatial cell on $-x$ inflow boundary whenever there are no wave packets in it. Injection coordinates are

$$x_{\mathrm{inj,L}} = \frac{1}{2} + \frac{V_{\mathrm{w}}}{\Delta x} t, \quad (13)$$

$$\lambda_{\mathrm{inj}} = \frac{1}{2}\left(\lambda_{\mathrm{l}} + \lambda_{\mathrm{l}+1}\right), \quad (14)$$

where t is the current simulation time. Injection position is clamped to be inside the inflow cell, $x_{\mathrm{inj,L}} \in [0, 1]$. The wave packets are injected to physical cell centroids $\lambda_{\mathrm{inj}} = \lambda_{\mathrm{l}} + 0.5\,\Delta\lambda$, instead of logical $\lambda_{\mathrm{L}} = \mathrm{l} + 0.5$ centroids, as this gives interpolated intensities that better correspond to the analytic intensities. The offset distance in Eqn. (13) maintains a constant distance Δx between subsequent wave packets. Injection energy is

$$U_{\mathrm{packet}} = \frac{\Delta x^3}{\mu_0}\int_{\lambda_{\mathrm{l}}}^{\lambda_{\mathrm{l}+1}} I(\lambda)\mathrm{d}\lambda. \quad (15)$$

Wave packets hitting the $+x$ outflow boundary are removed.

2.4.2. Shock Boundary Conditions

Waves crossing the shock front experience a jump in wavelength because $\mathbf{V}_{\mathrm{w}}$ in upstream and downstream regions differ. Incident waves also split into transmitted and reflected waves, conserving frequency and helicity. Boundary conditions discussed below are applied to the incident wave packets whenever a shock crossing is detected to create a transmitted wave, and a new reflected wave packet is injected to the simulation.

Transmitted (T) and reflected (R) wavelengths are given in terms of incident (I) wavelength as

$$\frac{\lambda^{\mathrm{R}}}{\lambda^{\mathrm{I}}} = \frac{V_{\mathrm{p},2} \mp V_{\mathrm{A},2} - V_{\mathrm{shock}}}{V_{\mathrm{p},1} \pm V_{\mathrm{A},1} - V_{\mathrm{shock}}}, \quad (16)$$

$$\frac{\lambda^{\mathrm{T}}}{\lambda^{\mathrm{I}}} = \frac{V_{\mathrm{p},2} \pm V_{\mathrm{A},2} - V_{\mathrm{shock}}}{V_{\mathrm{p},1} \pm V_{\mathrm{A},1} - V_{\mathrm{shock}}}, \quad (17)$$

where the upper (lower) signs hold for incident parallel (antiparallel) propagating waves.

Reflection (R) and transmission (T) coefficients for the wave amplitude $\delta\mathbf{B}$ are given in Campeanu and Schlickeiser (1992); Vainio and Schlickeiser (1998). For wave packet energies they are

$$R = \left\{ \frac{\sqrt{r}(\sqrt{r}-1)}{2} \frac{M_1+1}{M_1-\sqrt{r}} \right\}^2 \frac{\lambda^{\rm R}}{\lambda^{\rm I}}, \quad (18)$$

$$T = \left\{ \frac{\sqrt{r}(\sqrt{r}+1)}{2} \frac{M_1+1}{M_1+\sqrt{r}} \right\}^2 \frac{\lambda^{\rm T}}{\lambda^{\rm I}}, \quad (19)$$

where $M_1 = V_{\rm n1}/V_{\rm A1}$ is the Alfvénic Mach number in the upstream region. In Eqns. (18) and (19) the values in brackets are the reflection and transmission coefficients of wave intensities calculated in Campeanu and Schlickeiser (1992). The $\lambda^{\rm T,R}/\lambda^{\rm I}$ terms stem from the fact that in downstream region the wave packets are closer together than in upstream region. This effect is included in the intensity coefficients, but here we need to factor it out to avoid double-counting it.

2.5. Particles

Guiding center (GC) approximation is used for ions with state variables $(\mathbf{R}, V_\parallel, \mathcal{M})$, where $\mathcal{M} = \frac{1}{2}mv^2(1-\mu^2)/B_0$ is the magnetic moment. GC equations of motion are (Webb et al. 1983)

$$\frac{d\mathbf{R}}{dt} = \mathbf{V}_\parallel + \mathbf{V}_{\rm D}, \quad (20)$$

$$\frac{dV_\parallel}{dt} = -\frac{\mathcal{M}}{m}\nabla B_{0,\parallel} \quad (21)$$

$$+ \frac{\mathbf{V}_{\rm E}}{B_0} \cdot (\partial_t + \left[\mathbf{V}_\parallel + \mathbf{V}_{\rm E}\right] \cdot \nabla)\mathrm{B}_0, \quad (22)$$

$$\mathcal{M} = \text{constant}, \quad (23)$$

where the drift velocity

$$\mathbf{V}_{\rm D} = \mathbf{V}_{\rm E} + \mathbf{V}_{\nabla B} + \mathbf{V}_{\rm C} \quad (24)$$

$$= \frac{\mathbf{E}\times\mathbf{B_0}}{B_0^2} + \frac{\mathbf{B}_0 \times \nabla B_0}{B_0^2} \quad (25)$$

$$+ \frac{mV_\parallel^2}{q}\frac{\mathbf{B}\times(\mathbf{B}\cdot\nabla)\,\mathbf{B}}{B^4} \quad (26)$$

is the sum of electric, gradient, and curvature drifts. Electric field is the convectional $\mathbf{E} = -\mathbf{V}_{\rm p} \times \mathbf{B}_0$. Scattering also modifies ions' $\mathcal{M}$ and is handled in a separate step (see below).

2.5.1. Pitch-Angle Scattering

The quasilinear theory states that the pitch angle diffusion is governed by the $\mu-$dependent part of particle transport equation (Jokipii 1966),

$$\frac{\partial f}{\partial t} = \frac{\partial}{\partial \mu}\left(D_{\mu\mu}\frac{\partial f}{\partial \mu}\right) \quad (27)$$

$$= \frac{\partial^2 \left(D_{\mu\mu} f\right)}{\partial \mu^2} - \frac{\partial}{\partial \mu}\left(\frac{\partial D_{\mu\mu}}{\partial \mu} f\right). \quad (28)$$

Pitch angle diffusion coefficient in parallel or antiparallel wave rest frame $\mathbf{V}_{\rm w} = \mathbf{V}_{\rm p} \pm \mathbf{V}_{\rm A}$ (variables with tilde) is

$$D_{\mu\mu} = \frac{\pi}{2}\frac{\Omega}{B_0^2}\left(1-\tilde{\mu}^2\right)|k_{\rm res}|\, I(\mathbf{r}, k_{\rm res}) \quad (29)$$

$$= \frac{\pi}{2}\frac{\Omega}{B_0^2}\left(1-\tilde{\mu}^2\right)|\lambda_{\rm res}|\, I(\mathbf{r}, \lambda_{\rm res}), \quad (30)$$

evaluated at the resonant wavelength

$$\lambda_{\rm r} = 2\pi/k_{\rm r} = (2\pi/\Omega)\,\tilde{V}\tilde{\mu}. \quad (31)$$

The Fokker-Planck Eqn. (27) is formally equivalent to a stochastic differential equation

$$dX_t = a\,dt + b\,dW_t, \quad (32)$$

where drift $a = \partial_\mu D_{\mu\mu}$, variance $b^2 = 2D_{\mu\mu}$, W_t is a Wiener process, and $X_{\rm t}$ is the sought-after solution (particle pitch here). We proceed by solving Eqn. (32) using a first-order accurate implicit predictor-corrector method (Kloeden et al. 1997),

$$\tilde{\mu}_{\rm trial} = \tilde{\mu}_t + a(\tilde{\mu}_t)\,dt + b(\tilde{\mu}_t)\sqrt{dt}\,N, \quad (33)$$

$$a_0 = (1-\eta)\,a(\tilde{\mu}_t), \quad (34)$$

$$a_1 = (1-\eta)\,a(\tilde{\mu}_{\rm trial}), \quad (35)$$

$$\tilde{\mu}_{t+1} = \tilde{\mu}_0 + (\theta a_1 + (1-\theta)\,a_0)dt + (\eta b(\tilde{\mu}_t) + (1-\eta)\,b(\tilde{\mu}_{\rm trial})) \cdot\sqrt{dt}\,N, \quad (36)$$

where $\tilde{\mu}_{\rm t}$ and $\tilde{\mu}_{\rm t+1}$ are the initial and new pitch, and N is a normally distributed random number with zero mean and unit variance. We use values $\theta = 0$, $\eta = 0.5$, for the impliciteness parameters. Particles scattering outside the $|\tilde{\mu}| \leqslant 1$ interval are reflected at the boundaries, $\tilde{\mu} \to \tilde{\mu}' = 1 - \tilde{\mu}$.

The diffusion term b is interpolated to ion phase-space position as follows: first the intensity is interpolated in x to cell centroids neighboring the ion in λ direction, $I_l = S_i I_{il}$. Then diffusion

terms $b^2_{\rm L,U} = D_0(1-\mu^2_{\rm L,U})\left|\lambda^{\rm L,U}\right| I^{\rm L,U}$ are calculated, where $D_0 = \pi\Omega/\left(2B_0^2\right)$, on the upper (U) and lower (L) cell faces using average intensities $I^{\rm L} = \left(I_{l-1}+I_l\right)/2$, $I^{\rm U} = \left(I_l + I_{\rm l+1}\right)/2$. Finally, a and b terms are interpolated to ion position as

$$a = \frac{b^2_{\rm U} - b^2_{\rm L}}{2\left(\lambda_{l+1}-\lambda_l\right)}, \quad (37)$$

$$b^2 = b^2_{\rm L} + 2a\left(\lambda_{\rm r}-\lambda_l\right). \quad (38)$$

Thus, a is the derivative of b with respect to λ.

In principle the scattering algorithm, given in Eqns. (33)-(36), is limited by a Courant condition, i.e., ion should not cross multiple wavelength cells during a single scattering. This is unfeasible in practice, as a given change in pitch maps into larger and larger changes in λ as the particle energy increases (see Eqn. [31]). Noting that the wavelength cells are very small near $\lambda = 0$, and that $a \propto dt^{1/2}$, obeying Courant condition would result in prohibitely small time step.

Additional limitation to scattering time step comes from an analytic result of the Fokker-Planck Eqn. (27), namely that a time-independent solution must be a function of state variables (v,μ) only. In other words, an initially isotropic distribution in μ must stay isotropic at all times. The isotropicity condition forces the time step to be extremely small near $\tilde{\mu} = 0$ unless a and b are modified (see, e.g, Afanasiev and Vainio 2013, for discussion). Our modification is as follows: if $|\tilde{\mu}| < \tilde{\mu}_{\rm min}$, resonant wavelength is calculated using $\tilde{\mu}_{\rm min}$ instead of the correct $\tilde{\mu}$ when fetching the wave intensities above. This will "freeze" a to a constant value in the $|\tilde{\mu}| < \tilde{\mu}_{\rm min}$ interval, similarly to a technique used in Li et al. (2008); Mason et al. (2012). We use a value $\tilde{\mu}_{\rm min} = 0.025$ here.

Figure 1 shows modified drift and diffusion terms for a power law intensity for a 110 MeV proton. Wave intensity is the same as in the simulations discussed in Section 4. The drift term gets very large values near $\mu = 0$, which we effectively remove by "filling" the $\tilde{\mu} = 0$ resonance gap.

We impose a limitation that the maximum change in pitch is $\Delta\mu_{\rm max}$ during a single scattering, and substep the scatterer if the simulation time step $dt_{\rm sim}$ exceeds the maximum scattering time step. Scattering time step is evaluated as

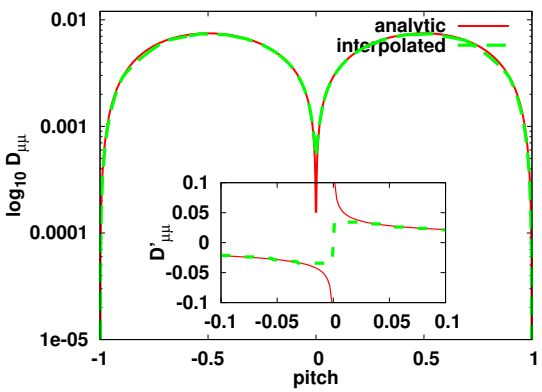

Fig. 1.— Interpolated (dashed, colored green in electronic edition) vs. analytic (solid, colored red in electronic edition) pitch angle diffusion coefficient $D_{\mu\mu}$ for wave intensity $I(k) = I_0\left(k/k_0\right)^{-5/3}$. Inset shows interpolated vs. analytic $\partial_\mu D_{\mu\mu}$ near $\mu = 0$, illustrating the effect of our modification. See the electronic edition of the Journal for a color version of this figure.

$$dt_{\rm max} = \min\left(\frac{\Delta\mu_{\rm max}}{a_{\rm max}}, \frac{\Delta\mu^2_{\rm max}}{b^2_{\rm max}}\right), \quad (39)$$

where $a_{\rm max}$ and $b_{\rm max}$ are estimates for maximum absolute values of the drift and diffusion terms that the particle can encounter. The number of substeps is $N_{\rm sub} = dt_{\rm sim}/dt_{\rm max}$. We precalculate the number of required substeps[1] for speeds $\tilde{V} \in 1.4\cdot\left[10^6, 10^7, 10^8, 10^9\right]$ m s^{-1} for all spatial cells. We then pick a suitable number of substeps for each particle based on the precalculated values. We keep track of the substeps the scatterer takes, and adjust $dt_{\rm sim}$ to keep $N_{\rm sub} \leqslant 10$.

2.5.2. Injection

The statistical weight W of a macroparticle is the number of real particles it represents within some energy and pitch intervals,

$$W = n(\mathbf{r})\Delta x^3 \int_U^{U+\delta U}\int_\mu^{\mu+\delta\mu} f(U,\mu)\,dU\,d\mu. \quad (40)$$

where $f(U,\mu) = (1/2)\,f_\kappa(U)\left[\theta(\mu+1)-\theta(\mu-1)\right]$, and θ is the step function.

[1]The relativistically incorrect speed of $1.4\cdot10^9$ m s^{-1} is only used to estimate the number of needed substeps.

Macroparticles are injected at a constant rate of N macroparticles per second. Thus, each time step only $N_{\rm inj} = N\Delta t$ macroparticles are injected, and the fractional part of $N\Delta t$ is used as a probability to inject an additional macroparticle. The injection energy interval is divided into $N_{\rm inj}$ uniformly spaced bins. Injected macroparticle gets a random energy in its bin, and a uniformly distributed random pitch $\mu \in [-1, +1]$. W is integrated using the bin limits in Eqn. (40).

The method described above gives a rather uniform distribution of particles over the injection energy range. If macroparticle U was randomized over the whole injection energy range instead of using the binning method, occasionally several low energy macroparticles could be generated, which would cause large (of the order of few) deviations from the correct number density. We also check statistical weights against spectral wave energies (see Section 2.7), and split injection ions as many times as necessary to keep the simulation stable.

2.6. Wave Growth Factors

A particle subject to scattering $\Delta\tilde{\mu}$ changes its energy in plasma frame by $\Delta U = mV_{\rm A}\tilde{V}\Delta\tilde{\mu}$, which must be removed from waves to conserve the total (particles+waves) energy. Resonant wavelength changes by $\Delta\lambda_{\rm r} = (2\pi/\Omega)\,\tilde{V}\Delta\tilde{\mu}$. Thus, the exchange energy per unit wavelength is

$$\Delta u = W\frac{mV_{\rm A}\Omega}{2\pi}. \qquad (41)$$

For each wavelength cell the particle fully crosses due to scattering, the wave energy changes by $\Delta U_{\rm w,l} = -\Delta u\Delta\lambda_{\rm l}$, where $\Delta\lambda_{\rm l}$ is the (physical) cell size. Each spatial cell receives an energy change $\Delta U_{il} = S_i\Delta U_{{\rm w},l}$, i.e., shape factors are only used in x direction. Partial wavelength cell crossings are accounted for in the same way, but the exact distance traveled is used instead of the full cell width $\Delta\lambda_{\rm l}$ when calculating $\Delta U_{\rm w,l}$.

After wave energy changes have been accumulated a diffusive smoothing is applied,

$$\frac{\delta\left(\Delta U_{\rm l}\right)}{\Delta\lambda_{\rm l}} = -D\left[\frac{\Delta U_{\rm l+1}}{\Delta\lambda_{\rm l+1}} - \frac{2\Delta U_{\rm l}}{\Delta\lambda_{\rm l}} + \frac{\Delta U_{\rm l-1}}{\Delta\lambda_{\rm l-1}}\right] \qquad (42)$$

with diffusion coefficient $D = 0.25$ to smooth out fluctuations due to numerical noise. Eqn. (42) is conservative, provided that diffusive fluxes are set to zero at the boundaries of wavelength mesh. Smoothing is done twice each time step before wave packet energies are modified.

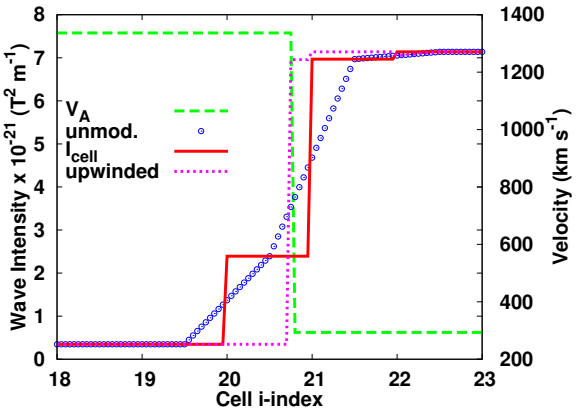

Fig. 2.— Interpolated wave intensity with (dotted, colored purple in electronic edition) and without (circles) shock sharpening vs. cell i-index. Shown are also wave intensity in cells (solid, colored red in electronic edition), and parallel Alfvén speed in shock normal incidence frame (dashed, colored green in electronic edition), which indicates the location of the shock front. See the electronic edition of the Journal for color version of this figure.

Finally, the energy changes are applied to wave packets. Each wave packet changes its energy by $\Delta U_{\rm packet} = S_{\rm il}\left(U_{\rm packet}/U_{\rm w,il}\right)\Delta U_{\rm w,il}$. The extra factor in parenthesis distributes the energy change $\Delta U_{\rm w,il}$ to all wave packets neighboring that phase-space cell ($U_{\rm w,il} = \sum_{\rm n} S_{\rm il}^{(n)} U_{\rm packet,n}$ is the accumulated sum of n wave packet energies).

2.7. Particle Splitters

We use two particle splitters in the simulation. The first one stabilizes the simulation by splitting macroparticles that have too large statistical weight relative to spectral wave energy. During the scattering process, a macroparticle can move anywhere within $\lambda \leqslant |\lambda_{\rm r,max}| = (2\pi/\Omega)\,\tilde{V}$ in λ direction. If the relative energy change in any wavelength cell, given by ratio (see Section 2.6)

$$R = \Delta u\Delta\lambda_{\rm l}/U_{\rm w,min}, \qquad (43)$$

where $U_{\rm w,min} = U_{\rm w}\left(|\lambda| \leqslant |\lambda_{\rm r,max}|\right)$ is the minimum wave energy the particle can encounter, is

too large, the scattering of a single macroparticle can remove a significant fraction of the wave energy from that cell or even cause the energy to become negative. If low wave energy regions are created, the tendency is for such regions to grow until all wave energy has been removed.

We periodically do a pass over spatial cells and check that macroparticles do not violate the condition $R \geqslant 0.01$. If it is, the macroparticle is split into 10 new identical particles with statistical weights $W/10$. This issue mostly concerns macroparticles that have a low injection energy and a large statistical weight, as low energy ions are more numerous. Alternatively, we could inject more low energy particles to keep W small.

A second particle splitter we use aims to improve resolution at high energies. We periodically bin the macroparticles based on their current simulation frame energy, and split particles if a bin contains too few particles.

2.8. Shock Sharpening

Pitch angle diffusion coefficients are calculated using interpolated wave intensities, while the wave speeds are calculated using analytic expressions (see Section 2.5.1). Interpolations incresed shock width to 3-4 spatial cell widths, as illustrated by the unmodified interpolation curve (symbols) in Figure 2. Problem this caused was that protons near the shock did not experience correct scattering center compression ratio. Thus, the first-order Fermi acceleration ended up being too slow and resulting proton power law indices were incorrect.

We solve this issue by upwinding (downwinding) particle shape factors if the particle is near the shock in the upstream (downstream) region. First, the spatial cell in which the shock front resides is calculated (i = 20 cell in Fig. 2). Then, shape factors are modified so that protons in neighboring cells (i $\in [19-21]$ in Fig. 2) do not use the wave intensity values in the shock cell (i = 20 in Fig. 2). Instead, the values are picked from the neighboring upstream (downstream) cell if the proton is in the upstream (downstream) region.

Related issue came up with the accumulation of wave energy changes and interpolations to wave packet positions (see Section 2.6). Consider protons scattering in the spatial cell immediately downstream of the shock ($i = 21$ in Fig. 2). If the protons accumulate wave growth factors to upstream side of the shock ($i = 19$, 20 cells in Fig. 2), those growth factors will be effectively multiplied by the wave transmission coefficient when the waves cross the shock front, leading to incorrect wave intensities in the downstream region.

We solved this in a similar manner for the intensity interpolations. Wave packets in the upstream region are only allowed to accumulate energy to upstream cells ($i \leqslant 20$ cells in Fig. 2), while wave packets in the downstream region can only accumulate to downstream cells ($i \geqslant 21$ in Fig. 2). Same condition is also applied when accumulating wave energy changes from proton positions to phase-space mesh, and when interpolating accumulated values to wave packet positions. Rest of the wave growth algorithm in Section 2.6 is unchanged. This solution prevents wave growth from being applied to wrong side of the shock front, while simultaneously conserving energy within roundoff errors.

3. Test Cases

3.1. Isotropicity

According to the Fokker-Planck Eqn. (27), an initially isotropic particle distribution in pitch must remain isotropic at all times. This property can be used to estimate the error of the scattering algorithm.

We test the isotropicity condition by evaluating a master equation for the scattering process as follows: a simulation is launched with a single spatial cell and wavelength mesh limits $\pm\lambda_{\max}$. Wave intensity is taken to be a power law. Wave packets are injected to the simulation, and their energies are accumulated to the simulation mesh to form the spectral intensity.

Consider particles having maximum resonant wavelengths $\lambda_{\mathrm{r,max}} = (2\pi/\Omega)\, V = C \cdot \lambda_{\max}$, where $C \in [0, 1]$ is a constant. Divide the pitch interval $\mu \in [-1, +1]$ into N bins of width $\Delta\mu = 2/N$, and form an N by N matrix A_{ij} for storing the results. For each column j, scatter M particles with a random pitch in interval $\mu_{\mathrm{j}} \leqslant \mu \leqslant \mu_{\mathrm{j}} + \Delta\mu$, and add each particle to row i of the matrix based on the new pitch μ' obtained from the scattering algorithm. The quantity $\delta M_j = \left(M - \sum_i A_{ij}\right)/M$ is the isotropicity error of the scattering algorithm.

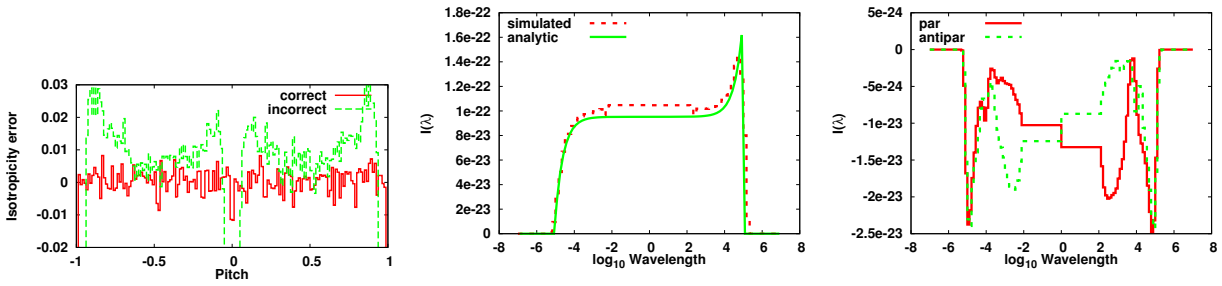

Fig. 3.— Left) Isotropicity error of first-order accurate predictor-corrector method with correct (solid, colored red in electronic edition) and incorrect (dashed, colored green in electronic edition) number of substeps. Middle) Simulated (dashed, colored red in electronic edition) spectrum of self-generated parallel Alfvén waves by isotropization of an initial beam distribution of protons vs. analytic result (solid, colored green in electronic edition). Right) Simulated parallel (solid, colored red in electronic edition) and antiparallel (dashed, colored green in electronic edition) self-generated wave spectra for second-order Fermi acceleration. See the electronic edition of the Journal for color versions of these figures.

Figure 3a shows the isotropicity error for 110 MeV protons using $M = 100000$ particles and $N = 160$ bins. Wave intensity was the same as that used in DSA simulations 1-3 (see Section 4). Simulation time step was set to 10 seconds, but the adaptive time step control set the scatterer dt to 0.02849 seconds (351 substeps). Figure 3a also shows corresponding results but with incorrect (10) number of substeps. The scattering algorithm, with substepping enabled, is able to maintain isotropicity extremely well.

3.2. Self-Generated Wave Spectra

Alfvén wave spectrum generated by isotropization of a beam distribution ($\tilde{\mu} = 1$ in parallel Alfvén wave rest frame) is given by (Schlickeiser et al. 2002; Afanasiev and Vainio 2013)

$$I(k) = 2\pi n V_{\rm A} \frac{p\Omega}{Vk^2}\left(1+\frac{\Omega}{kV}\right), \quad (44)$$

$$I(\lambda) = \frac{\mu_0 n V_{\rm A} p}{2\lambda_{\rm r,max}}\left(1+\frac{\lambda}{\lambda_{\rm r,max}}\right). \quad (45)$$

Eqn. (45) represents a simple triangle pulse constrained to interval $|\lambda| \leqslant \lambda_{\rm r,max}$. Self-generated wave spectra from simulations are in very good agreement with the analytic result (see Figure 3b). Results were produced by running the simulation with a single spatial cell and applying periodic boundary conditions. Total (wave+particle) energy is conserved within roundoff errors.

Figure 3c shows self-generated wave spectra in a similar setup as above, but with equal initial parallel and antiparallel Alfvén wave background. Monoenergetic (86.2 keV, 2.26 μT magnetic field, $n = 9.085 \cdot 10^{10}$ m^{-3} plasma number density) protons had initially an isotropic distribution in pitch in plasma rest frame. It is not possible to reach distribution that is isotropic in both wave rest frames simultaneously, because the waves move to opposite directions. The second-order Fermi process will, on average, continuously accelerate particles, and damp both wave modes. Resulting self-generated wave spectra have very pronounced "spikes" at long ($\propto \lambda_{\rm r,max}$) wavelengths, and are antisymmetric with each others over $\lambda = 0$ point.

This setup is extremely sensitive to numerical noise due to finite number of macroparticles in the spatial cell. Fig. 3c was produced by averaging results from ten identical simulations that had different random number generator seeds.

4. Results

4.1. Setup

DSA simulations were run with parameters suitable for the solar corona near 10 solar radii ($R_{\rm sun}$). Two-dimensional simulation box was taken to extend from -10 to +10 solar radii in x-direction, and from -10^7 to $+10^7$ m in wavelength with $\lambda_0 = 1000$ m. Upstream plasma number density was set to $n_0 = 9.085 \cdot 10^{10}$ m^{-3},

Run	Scat.[a]	$C^{+b}_{L,R}$	Wave gen.[c]	AP[d]
1	I	$3 \cdot 10^{-3}$	N	N
2	A	$3 \cdot 10^{-3}$	N	N
3	A	$3 \cdot 10^{-3}$	Y	Y
4	A	$6 \cdot 10^{-3}$	Y	Y
5	A	$9 \cdot 10^{-3}$	Y	Y

Table 1: Summary of simulation runs presented in this manuscript. a) Scattering model used: isotropic (I) or anisotropic (A). b) Normalization constant of ambient parallel Alfvén wave power spectrum. c) Were protons allowed to self-generate waves (Y for yes, N for no)? d) Were reflected antiparallel Alfvén waves created at the shock?

velocity 1500 km s^{-1} in shock rest frame, and magnetic field 2.26 μT, roughly corresponding to the values of coronal model by Mann et al. (2003) at 10 R_{sun}. In the simulation box the shock is centered at $x = 2.45$ R_{sun}. Shocks in corona are typically strong, having gas compression ratios above 3.5 near CME nose regions. Here we simply use a constant gas compression ratio $R_{gas} = 4$.

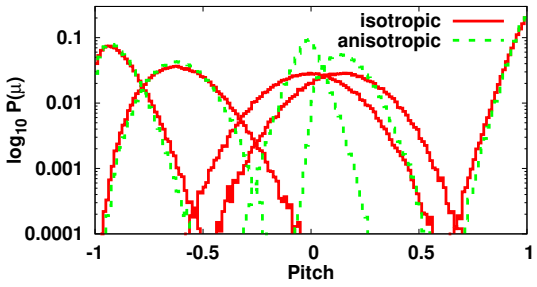

Fig. 4.— Comparison of scattering probability densities between isotropic (solid, colored red in electronic edition) and anisotropic (dashed, colored green in electronic edition) scattering operators for 110 MeV protons with several initial pitch values (not shown) for Kolmogorov wave spectrum. For initial pitch $\tilde{\mu} = \pm 1$ the probability densities are almost equal, but the differences grow larger when initial pitch $\tilde{\mu} \to 0$. Isotropic scattering is always more efficient at scattering particles. See the electronic edition of the Journal for a color version of this figure.

Parallel-propagating Alfvén wave packets were injected to $-x$ inflow boundary at a constant rate. A Kolmogorov wave intensity with $k-$spectral index of $-5/3$ was used, and both helicities were separately normalized against ambient magnetic field energy density with a normalization constant $C^{+}_{L,R}$ over the wavelength range $0 \leqslant |\lambda_{max}| \leqslant 4{\cdot}10^8$ m. To set up the wave background, the simulation was run with Alfvén waves only for 40000 seconds. Initially, the parallel mean free path in runs 1-3, (Hasselmann and Wibberenz 1970)

$$d_{\parallel} = \frac{3\,v}{8} \int_{-1}^{+1} \frac{(1-\mu^2)}{D_{\mu\mu}} d\mu = 3D_{\parallel}/v, \qquad (46)$$

was 5.72R_{sun} in the upstream region, and 0.17R_{sun} in the downstream region for 0.16-0.32 MeV protons with the chosen parameters. In Eqn. (46) $D_{\parallel}$ is the parallel diffusion coefficient.

In shock rest frame, parallel wave speed in upstream region in 1336 km s^{-1}, and 293.2 km s^{-1} in downstream region, while antiparallel wave speed is 456.8 km s^{-1} in downstream region. Numerically, the transmission and reflection coefficients for incident wave intensity at constant λ, are 32.2 and 1.1, which are equal to those obtained from Eqns. (20-21) in Vainio and Schlickeiser (1998).

After wave background was set up, monoenergetic (1000 Maxwell-Boltzmann thermal energy, 86.2 keV) protons were injected directly in front of the shock. Particles with velocity vectors pointing away from the shock were rejected. Macroparticle weights were using Eqn. (2) with a kappa-index $\kappa = -3$. We ended up multiplying the injected particle weights by 50000 in all simulation runs to clearly demonstrate the effects of the wave generation, as the kappa distribution has very few suprathermals at high energies. The scaled suprathermal number density was $\sim 0.0088 \cdot n_0$. Simulations were then run for 8000 seconds with various features turned on or off (see Table 1).

In order to have a comparison against previous modeling efforts, we ran the same setup using both anisotropic and isotropic pitch angle scattering operators. Main difference between the operators is that in isotropic scattering, the particle pitch is neglegted in resonance condition, i.e., $D_{\mu\mu}$ is evaluated using $\lambda_{r,max}$ instead of $\lambda_{r,max}\,|\tilde{\mu}|$. We chose an isotropic scattering algorithm that has been used in several previous studies (e.g., Jones and Ellison 1991; Torsti et al. 1996).

Figure 4 shows probability densities for isotropic

and anisotropic scattering for several initial pitch values (correspond to peak values of each curve). For each initial $\tilde{\mu}$, the vertical axis gives the probability of scattering to that $\tilde{\mu}$ over the used time step. Isotropic scattering is more efficient at diffusing particles across the $\tilde{\mu} = 0$ resonance gap.

4.2. Energy Spectra

Figure 5 shows proton energy spectra vs. position at the end of simulation runs 1,2, and 4. Left and middle panels show energy spectra from simulation run where isotropic (run 1) and anisotropic (run 2) scattering operator was used. As expected, isotropic scattering is more effective in trapping protons near the shock front, and the maximum energies end up being higher than with anisotropic scattering. Ultimately, the maximum proton energies are limited by the size of the simulation box, i.e., the $\pm x$ walls are free escape boundaries.

The right panel of Fig. 5 shows energy spectra from run 4, where antiparallel wave creation at the shock was turned on, i.e., both first and second-order Fermi acceleration are operating in this run. Most notable difference to run 2 is the flattening of energy spectra below ~ 100 keV due to second-order Fermi acceleration in the downstream region.

Analytical solutions to similar scenarios than in our simulations exist, although typically some simplifying assumptions are needed, for example, for diffusion coefficients, to obtain a solution in closed form. According to Webb (1983), if spatial diffusion coefficients are independent of momentum, and the momentum diffusion coefficient related to second-order Fermi acceleration decreases exponentially from the shock in the downstream region, a steady-state momentum distribution in the upstream region is given by

$$F_0(x,p) = F_0(0,p)\exp(V_{\mathrm{w},1}x/D_{\parallel}), \qquad (47)$$

where $F_0(0,p)$ is the isotropic part of proton distribution at the shock. Thus, distribution at constant momentum should decrease exponentially with increasing distance Δx to the shock with an e-folding distance

$$d = \frac{V_{\mathrm{w},1}\Delta x}{D_{\parallel}} = \frac{3V_{\mathrm{w},1}\Delta x}{v\, d_{\parallel}}. \qquad (48)$$

Figure 6 shows momentum spectra at ~ 240 keV at the end of our simulation runs vs. distance to the shock. Simulated spectra are in good agreement with the exponential decrease predicted by Eqn. (47) until boundary effects start to dominate, i.e., particles hitting $-x$ boundary get removed from the simulation. By using values from simulation run 3, $\Delta \ln F(p) \approx 5.3$, $\Delta x \approx 1.1 \cdot 10^{10}$ m, $V_{\mathrm{w},1} = 1336$ km s^{-1}, and $v = 6800$ km s^{-1} for 240 keV protons, the mean free path according to Eqn. (48) should be $d_{\parallel} \approx 1.7\, R_{\mathrm{sun}}$, which is lower than the actual 5.72 R_{sun} mean free path in our simulations.

Enhanced distributions ("bumps") in the downstream region near $x \sim 4 \cdot 10^9$ m in runs 3-5 (see Fig.6), are due to limited simulation time. At downstream parallel wave speed of 293.2 km s^{-1}, waves self-generated immediately after proton injection have moved to $x \approx 4.06 \cdot 10^9$ m during 8000 s (shock is located at $x \approx 1.71 \cdot 10^9$ m).

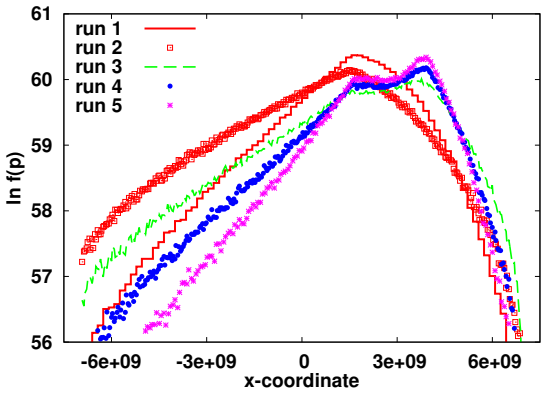

Fig. 6.— Proton momentum distribution at ~ 240 keV vs. x-coordinate at the end of simulation runs 1-5. In all cases the proton spectra decrease exponentially with increasing distance to the shock until boundary effects start to dominate. See the electronic edition of the Journal for a color version of this figure.

There are many factors that may contribute to the difference between the analytic result and order-of-magnitude estimate above. For example, wave generation somewhat decreases mean free paths near the shock, $\Delta \ln F_0(p)$ above was calculated using total proton distribution instead of the isotropic part, assumptions made by Webb (1983) do not apply for our model, and the dis-

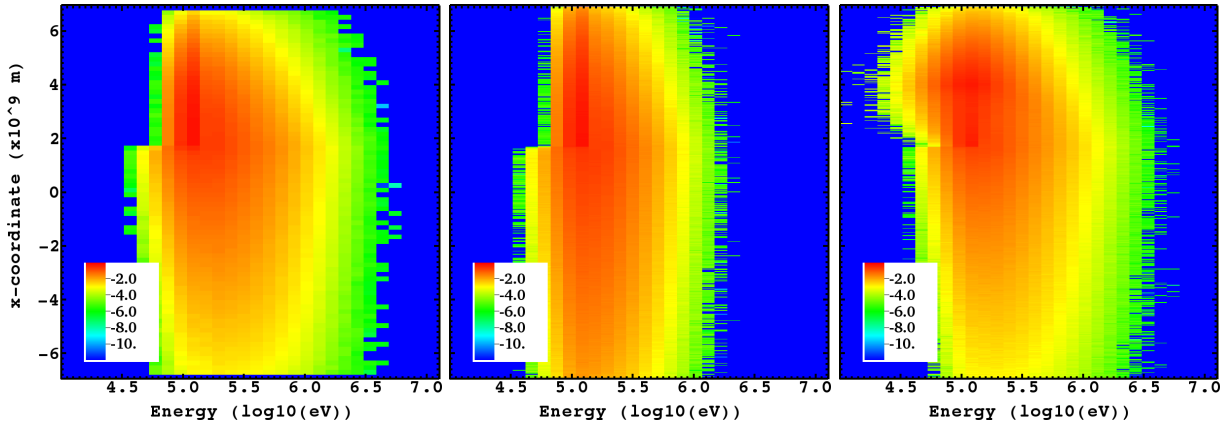

Fig. 5.— Left) Proton energy spectra ($1/\mathrm{m}^3\mathrm{eV}$) vs. x-coordinate at the end of simulation run 1 for isotropic scattering and parallel propagating Alfvén waves only. Middle) Same as left panel, but for run 2 where anisotropic scattering was used. Isotropic scattering is more effective at diffusing ions across the resonance gap, and thus overestimates the rate of diffusive shock acceleration. Right) Same as middle panel, but for run 4 where reflected antiparallel Alfvén waves were created and wave self-generation was turned on. The shock is located near $x = 1.71 \cdot 10^9$ m in all panels. See the electronic edition of the Journal for a color version of this figure.

tance (in mean free paths) between the shock and free escape boundary depends on proton momentum. Considering that, the simulations are in good agreement with the analytic result.

Well-known result of first-order Fermi acceleration is that the particle spectrum in the dowstream region is a power law (Axford et al. 1977; Krymskii 1977; Bell 1978; Blandford and Ostriker 1978)

$$f(U) \propto (U/U_0)^{-q}, \qquad (49)$$

where the spectral index $q = (r+2)/(r-1) = -1.84$ depends only on the scattering center compression ratio $r = V_{\mathrm{w},1}/V_{\mathrm{w},2} = 4.56$. If the time available for acceleration is limited or there are free escape boundaries, the energy spectra typically show an exponential cutoff at some energy. Figure 7 shows proton energy spectra immediately downstream of the shock at $x = 2{\cdot}10^9$ m from runs 1-5. Spectrum from the isotropic run 1 is in good agreement with the analytic prediction at lower energies until it starts to soften above ~ 1 MeV, indicating that protons at these energies are escaping the acceleration region. Anisotropic runs need over twice as large ambient wave intensity to reach the same acceleration efficiency.

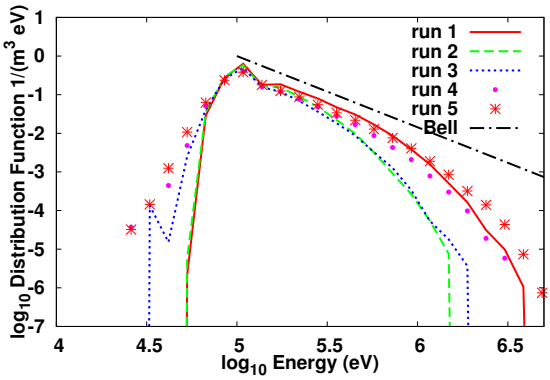

Fig. 7.— Proton energy spectra in the downstream region at $x = 2 \cdot 10^9$ m from simulation runs 1-5 vs. analytic prediction (dash-dotted, colored black in electronic edition). See the electronic edition of the Journal for a color version of this figure.

4.3. Self-generated Waves

Figure 8 (solid line) shows the self-generated parallel and antiparallel wave spectra at the end of simulation run 4. The characteristic triangle pulse (Sec. 3.2) is clearly visible in all spectra. Note the lack of resolution below $|\lambda| \leqslant \lambda_0 = 1$ km

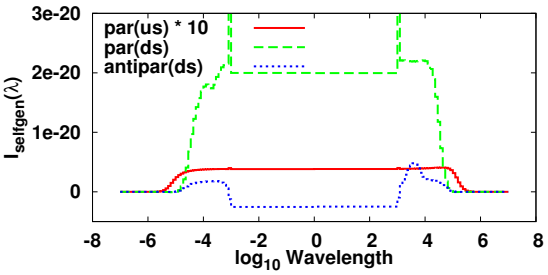

Fig. 8.— Self-generated wave spectra at the end of simulation run 4. Shown are parallel Alfvén spectra immediately upstream ($x = 1.5 \cdot 10^9$, solid, colored red in electronic edition) and downstream ($x = 2 \cdot 10^9$ m, dashed, colored green in electronic edition) of the shock, and antiparallel Alfvén spectrum downstream of the shock (dotted, colored blue in electronic edition). The spikes in upstream spectrum at $\lambda = \pm 10^3$ m are due to changing cell sizes in wavelength mesh. See the electronic edition of the Journal for a color version of this figure.

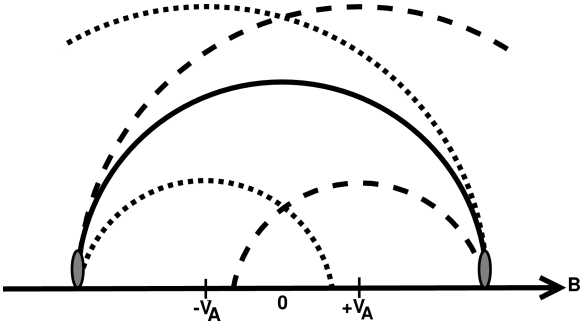

Fig. 9.— Scattering circles for isotropization of initial beam $\tilde{\mu} = \pm 1$ distribution (gray ovals). In parallel Alfvén rest frame ($V = +V_A$) scattering is elastic, and ions move along circles (dashed line). If the circle in wave rest frame has a smaller (larger) radius than in plasma rest frame (solid line), ions lose (gain) energy and waves are amplified (damped). Corresponding results are shown for antiparallel waves (dotted lines).

wavelengths. Various spectral features in Fig. 8 can be understood by considering the "scattering circles" shown in Fig. 9, which illustrates when wave decay and amplification occur for an initially beam distribution.

Injected particles initially have an anisotropic $\tilde{\mu} < 0$ pitch distribution immediately to the downstream of the shock, thus isotropization of the transmitted particles damps parallel R-helicity Alfvén waves, meaning that the peak of self-generated wave spectrum is located on negative (R-helicity) wavelengths (see Fig. 3a). In Fig. 9 this roughly corresponds to the gray oval on left.

A fraction of injected particles scatter to $\tilde{\mu} > 0$ half-plane and diffuse back to the upstream region, where the isotropization now amplifies parallel waves (gray oval on right in Fig. 9), and a triangular pulse is created (solid curve in Fig.8). When the amplified waves transmit through the shock, intensity is amplified, and the width of the pulse reduces by a factor of $\lambda^{\mathrm{T}}/\lambda^{\mathrm{I}}$ (dashed curve in Fig. 8). Incident self-generated waves also create antiparallel waves with same helicities and spectral shape in the downstream region, but at slightly longer wavelengths (Fig. 8, dotted curve).

For antiparallel Alfvén waves in the downstream region the situation is more complex, as there are several effects operating simultaneously. First, isotropization of transmitted ions amplifies R-helicity waves (opposite effect to parallel waves, see Fig. 9). In our simulations this occurs within $\sim 5 \cdot 10^8$ m to the shock. Further into the downstream region, antiparallel waves are damped in second-order Fermi acceleration.

Figure 10 shows parallel wave intensity at $\log \lambda = 5$ vs. x-coordinate at 4000 and 8000 seconds into the simulation from run 3. In the upstream region we see that the foreshock extends several solar radii from the shock front, and becomes more pronounced as protons generate more waves. In downstream region parallel wave intensity stays almost flat, while antiparallel waves are somewhat damped as discussed above.

5. Summary

We have presented a new numerical model for diffusive shock acceleration of ions. The described model includes propagation of parallel and antiparallel slab mode Alfvénic turbulence, transmission of waves through the shock, and self-consistent wave amplification due to the accelerating ions. The wave-particle interaction is through gyro resonance. Waves are treated in a similar fashion as energetic particles. The new model uses the full form of quasilinear pitch angle scatter-

ing resonance condition, which is a more realistic description than the simpler isotropic scattering approach used in previous studies, and is in good agreement with analytic solutions of diffusive shock acceleration.

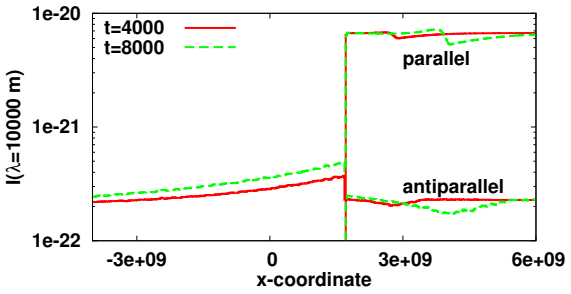

Fig. 10.— Parallel Alfvén wave intensities at $\lambda =$ 100 km vs. x-coordinate 4000 (solid, colored red in electronic edition) and 8000 (solid, colored green in electronic edition) seconds after proton injection started from simulation run 3 where both wave modes were included. Shown are also antiparallel wave intensities at same values of time (dashed). See the electronic edition of the Journal for a color version of this figure.

We have applied the new model to acceleration of protons at parallel shocks using parameters suitable for solar corona near ten solar radii. We find that there is a significant difference in efficiency of first-order Fermi acceleration between isotropic and anisotropic scattering. Isotropic scattering predicts much higher acceleration rate as compared with the more realistic anisotropic scattering due to shorter particle mean free paths. We find that anisotropic scattering requires over twice as large ambient turbulence in order to reach the same acceleration efficiency. With the parameter range considered in this study, protons are accelerated to a few MeV energies. In the future we plan to extend the model to a more general geometry.

Although the number of suprathermal protons at ten solar radii seems to be too small for notable wave generation, the resulting wave intensities show clear deviations from a power law shape near maximum resonant wavelengths of 30-300 km, especially in the downstream region. These waves are created by energetic protons that transmitted through the shock from the downstream to upstream region, where the isotropization of streaming protons most efficiently amplifies Alfvén waves with wave vectors pointing away from the shock front. The amplified upstream waves are transmitted through the shock front, where the compression of wave magnetic field increases the intensity by a factor of ~ 32. Jump in wave speed at the shock causes reflected waves to be created in the downstream region, that have the same spectral structure as the incident upstream waves but wave vectors pointing to the opposite direction.

Wave reflection at the shock enables second-order Fermi acceleration, and decreases proton mean free paths in the downstream region, somewhat increasing the efficiency of first-order Fermi acceleration. Second-order Fermi acceleration, according to our simulations, is generally too weak process to have a notable effect on the high energy ions. However, the effect on low energy ($\leqslant$ 100 keV) ions is significant, causing considerable flattening of energy spectra. Additionally, we find that waves in the downstream region are very efficiently damped by particles, which may be an important mechanism for heating suprathermal protons. A detailed study of this process is, however, beyond the scope of this manuscript.

Corsair is a parallel simulation platform, suitable for domain-decomposed mesh and particle-mesh simulations. Corsair, and the Corsair/SEP shock acceleration model, are available under GNU general public license, and can be obtained by contacting AS. Simulations presented here were carried out on Finnish Meteorological Institute's Cray XT5c supercomputer using 100 CPU cores.

The work of AS was funded by Academy of Finland grant 251797. The work at University of Alabama in Huntsville is supported by NSF ATM-0847719.

REFERENCES

A. Afanasiev and R. Vainio. Monte Carlo Simulation Model of Energetic Proton Transport through Self-generated Alfvén Waves. *ApJS*, 207:29, August 2013.

W. I. Axford, E. Leer, and G. Skadron. The acceleration of cosmic rays by shock waves. *Proc. 15th Internat. Cosmic Ray Conf. (Plovdiv)*, 11: 132–137, 1977.

M. Battarbee, T. Laitinen, and R. Vainio. Heavy-

ion acceleration and self-generated waves in coronal shocks. *A&A*, 535:A34, November 2011.

A. R. Bell. The acceleration of cosmic rays in shock fronts. I. *MNRAS*, 182:147–156, January 1978.

C. K. Birdsall and A. A. Langdon. Plasma physics via computer simulation. *New York: McGraw-Hill*, 1985.

R. D. Blandford and J. P. Ostriker. Particle acceleration by astrophysical shocks. *ApJ*, 221: L29–L32, April 1978.

A. Campeanu and R. Schlickeiser. Alfven wave transmission and stochastic particle acceleration at parallel astrophysical shock waves. *A&A*, 263:413–422, September 1992.

R. B. Decker. Computer modeling of test particle acceleration at oblique shocks. *Space Sci. Rev.*, 48:195–262, 1988.

D. C. Ellison, S. P. Reynolds, and F. C. Jones. First-order Fermi particle acceleration by relativistic shocks. *ApJ*, 360:702–714, September 1990.

J. Giacalone. Particle Acceleration at Shocks Moving through an Irregular Magnetic Field. *ApJ*, 624:765–772, May 2005.

K. Hasselmann and G. Wibberenz. A Note on the Parallel Diffusion Coefficient. *ApJ*, 162:1049, December 1970.

R. W. Hockney and J. W. Eastwood. Computer simulation using particles. *CRC Press*, 1989.

J. R. Jokipii. Cosmic-Ray Propagation. I. Charged Particles in Random Magnetic Field. *ApJ*, 146: 480, November 1966.

J. R. Jokipii. Rate of energy gain and maximum energy in diffusive shock acceleration. *ApJ*, 313: 842–846, February 1987.

F. C. Jones and D. C. Ellison. The plasma physics of shock acceleration. *Space Sci. Rev.*, 58:259–346, December 1991.

P. E. Kloeden, E. P. Platen, and H. Schurz. Numerical solution of SDE through computer experiments. *Springer-Verlag*, 1997.

G. F. Krymskii. A regular mechanism for the acceleration of charged particles on the front of a shock wave. *Dokl. Akad. Nauk SSSR*, 234: 1306–1308, June 1977.

G. Li, G. P. Zank, and W. K. M. Rice. Energetic particle acceleration and transport at coronal mass ejection-driven shocks. *J. Geophys. Res.*, 108:1082, February 2003.

G. Li, G. P. Zank, and W. K. M. Rice. Acceleration and transport of heavy ions at coronal mass ejection-driven shocks. *J. Geophys. Res.*, 110:A06104, June 2005.

G. Li, Q. Hu, O. Verkhoglyadova, G. P. Zank, R. P. Lin, and J. Luhmann, editors. *Particle acceleration and transport in the heliosphere and beyond:7th Annual International Astrophysics Conference*, volume 1039 of *American Institute of Physics Conference Series*, October 2008.

G. Mann, A. Klassen, H. Aurass, and H.-T. Classen. Formation and development of shock waves in the solar corona and the near-Sun interplanetary space. *A&A*, 400:329–336, March 2003.

G. M. Mason, G. Li, C. M. S. Cohen, M. I. Desai, D. K. Haggerty, R. A. Leske, R. A. Mewaldt, and G. P. Zank. Interplanetary Propagation of Solar Energetic Particle Heavy Ions Observed at 1 AU and the Role of Energy Scaling. *ApJ*, 761:104, December 2012.

C. K. Ng and D. V. Reames. Shock Acceleration of Solar Energetic Protons: The First 10 Minutes. *ApJ*, 686:L123–L126, October 2008.

C. K. Ng, D. V. Reames, and A. J. Tylka. Effect of proton-amplified waves on the evolution of solar energetic particle composition in gradual events. *Geophys. Res. Lett.*, 26:2145–2148, 1999.

C. K. Ng, D. V. Reames, and A. J. Tylka. Modeling Shock-accelerated Solar Energetic Particles Coupled to Interplanetary Alfvén Waves. *ApJ*, 591:461–485, July 2003.

D. V. Reames and C. K. Ng. Streaming-limited Intensities of Solar Energetic Particles. *ApJ*, 504:1002, September 1998.

A. Sandroos and R. Vainio. Particle acceleration at shocks propagating in inhomogeneous magnetic fields. *A&A*, 455:685–695, August 2006.

A. Sandroos and R. Vainio. Simulation Results for Heavy Ion Spectral Variability in Large Gradual Solar Energetic Particle Events. *ApJ*, 662: L127–L130, June 2007.

R. Schlickeiser, R. Vainio, M. Böttcher, I. Lerche, M. Pohl, and C. Schuster. Conversion of relativistic pair energy into radiation in the jets of active galactic nuclei. *A&A*, 393:69–87, October 2002.

J. Torsti, L. G. Kocharov, R. Vainio, A. Anttila, and G. A. Kovaltsov. The 1990 May 24 Solar Cosmic-Ray Event. *Sol. Phys.*, 166:135–158, June 1996.

A. J. Tylka and M. A. Lee. A Model for Spectral and Compositional Variability at High Energies in Large, Gradual Solar Particle Events. *ApJ*, 646:1319–1334, August 2006.

R. Vainio and T. Laitinen. Monte Carlo Simulations of Coronal Diffusive Shock Acceleration in Self-generated Turbulence. *ApJ*, 658:622–630, March 2007.

R. Vainio and R. Schlickeiser. Alfven wave transmission and particle acceleration in parallel shock waves. *A&A*, 331:793–799, March 1998.

R. Vainio, L. Kocharov, and T. Laitinen. Interplanetary and Interacting Protons Accelerated in a Parallel Shock Wave. *ApJ*, 528:1015–1025, January 2000.

G. M. Webb. First order and second order Fermi acceleration of energetic charged particles by shock waves. *ApJ*, 270:319–338, July 1983.

G. M. Webb, W. I. Axford, and T. Terasawa. On the drift mechanism for energetic charged particles at shocks. *ApJ*, 270:537–553, July 1983.

G. B. Whitham. A general approach to linear and non-linear dispersive waves using a Lagrangian. *J. Fluid. Mech.*, 22:273–283, 1965.

G. P. Zank, W. K. M. Rice, and C. C. Wu. Particle acceleration and coronal mass ejection driven shocks: A theoretical model. *J. Geophys. Res.*, 105:25079–25096, November 2000.

This 2-column preprint was prepared with the AAS LaTeX macros v5.2.